Synthesis and Photothermal Properties of UV-Plasmonic Group IV Transition Metal Carbide Nanoparticles.

Matthew J. Margeson,[a] Yashar E. Monfared[a] and Mita Dasog[a]*

[a]Department of Chemistry, Dalhousie University, Halifax, Nova Scotia, Canada

*Email: mita.dasog@dal.ca

Abstract

Refractory nanostructures are low-cost and chemically and thermally robust alternatives to noble metal based plasmonic materials. Transition metal nitrides have received much of the attention lately, but there has been less emphasis on closely related non-layered carbide counterparts. In this work, plasmonic group IV transition metal carbide (TiC, ZrC, and HfC) nanostructures were prepared using a facile magnesiothermic reduction method which yielded phase pure product. TiC, ZrC and HfC with rock salt crystal structure and an average particle size of 24, 31, and 42 nm, respectively were obtained by reacting corresponding metal oxide, magnesium, and biochar in solid-state. Calculations performed using finite element method predicted these group IV carbide nanostructures to have localized surface plasmon resonance in the UV region between 150 – 175 nm. The photothermal transduction efficiency of each carbide was explored to further verify the plasmonic behavior. HfC was found to have the highest photothermal transduction efficiency (73%), followed by ZrC (69%), and then TiC (60%) at 365 nm.

Keywords

Transition metal carbide

Plasmonics

Solid-state synthesis

Biochar

Photothermal

Introduction

Plasmonic materials are known for their ability to drastically enhance light-matter interactions resulting in strong light absorption and scattering, enhanced local electric fields, and heat generation.[1–5] This occurs via the excitation of free electrons known as surface plasmons, the existence of which can be predicted by negative dielectric permittivity in the optical frequency range.[6,7] Unlike conventional optics, plasmonic materials enable unrivalled concentration of light beyond the diffraction limit.[8,9] Recent developments into plasmonic nanomaterials have created research interest in using them for sensing,[10,11] data recording and storage,[12] improved energy harvesting,[13,14] solar-vapor conversion,[15–19] photocatalysis[14,20,21] and photothermal therapy.[22–24] Traditional plasmonic materials like gold and silver have suffered from thermal instability due to low bulk melting points, chemical instability, and/or high cost.[25] It has become clear from the past few decades of research that practical devices will require engineering new materials which address the underlying issues of the existing plasmonic nanomaterials. Alternative materials ranging from refractories to complex oxides and intermetallics have been suggested as potential replacements for noble metals.[26,27]

Refractory nanomaterials are envisioned to be suitable for plasmonic applications as they display absorption throughout the solar spectrum, from the UV to the NIR regimes depending on their composition and morphology.[28,29] Based on the bulk material characteristics, they are also predicted to be chemically stable for operation under corrosive conditions.[30] They have high melting points compared to metals making them compatible with the high temperature fabrication processes.[31] Refractory transition metal nitrides have been shown to have high photothermal efficiency, thermal stability, and catalytic activity.[19,32,33] While reports on plasmonic nitride nanoparticles (NPs) have soared over the past few years, there has yet to be detailed investigation

into the optical properties of their close relative, non-layered transition metal carbides (TMCs). Numerical calculations performed on 100 nm spherical TiC, ZrC, and HfC NPs showed them to possess localized surface plasmon resonance (LSPR) in the blue-UV region of the electromagnetic spectrum.[34] More recently, commercially purchased 50 nm ZrC particles were used for solar-driven water evaporation process.[35] These particles had LSPR in the UV region and exhibited superior photothermal properties. While this report shows the promise of plasmonic carbides, detailed experimental methods exploring their synthesis and plasmonic properties remain scarce.

Herein, we report the solid-state synthesis of group IV transition metal carbide (TiC, ZrC, and HfC) NPs using a magnesiothermic reduction reaction and biochar as the carbon source. The optical properties were investigated experimentally and calculated using finite element method. The photothermal transduction efficiency at 365 nm was determined for TiC, ZrC, and HfC suspended in water.

Experimental Section

Materials. Titanium dioxide (TiO_2 99.9%, 18 nm), zirconium dioxide (ZrO_2, 99.95%, 20nm), and hafnium dioxide (HfO_2, 99.95%, 61-80 nm) were purchased from U.S. Research Nanomaterials. Magnesium powder (Mg, 99.8%, 325 mesh) was purchased from Alfa Aesar. Hydrochloric acid (HCl, ≥99%), and nitric acid (HNO_3, ≥99%) were purchased from Sigma-Aldrich. Deionized water (DI-water, 18.2 MΩ) was obtained from a Sartorius Arium water purification system. All chemicals were used as received without further purification.

Synthesis of biochar. Biochar was prepared using a previously reported anaerobic pyrolysis process.[36] Briefly, debarked birch wood was pyrolyzed at 400 °C for 30 minutes in a tube furnace

under N_2 atmosphere and quenched in cold water. Biochar (200 g) was then transferred to a 500 mL beaker equipped with a magnetic stir-bar and to which deionized H_2O (200 mL) was added. The mixture was heated to a boil and allowed to stir for 15 minutes. The biochar was collected via filtration and the solid product was washed with water until the filtrate ran clear. The resulting biochar was dried in an oven at 100 °C for 2 days. The dried carbon product was ground for 10 minutes and finally sieved to a particle size of ~150 μm. The sieved biochar (2.0 g) was then added to a beaker equipped with a magnetic stir-bar and reacted with concentrated HNO_3 (aq) (68%, 10 mL) for 30 minutes. Afterwards, the reaction was filtered, and the acid-treated biochar was rinsed with deionized water until the filtrate was neutral. The biochar was again dried in an oven at 100 °C for 2 days.

Synthesis of transition metal carbides

Titanium carbide (TiC). TiO_2 (200 mg, 3.75 mmol) and biochar (90.2 mg, 7.51 mmol) powders were mixed well using a mortar and pestle. To this mixture Mg powder (365 mg, 15.0 mmol) was added and ground inside a N_2 filled glovebox until homogeneous mixture of all three reagents was obtained. The resulting mixture was transferred to a Coors^{TM} high alumina combustion boat and placed into a quartz tube and purged with Ar for 15 minutes in a Lindberg Blue MTM furnace. After this, the reaction was heated to 950 °C at a rate of 10 °C·min^{-1} and held at that temperature for 4 hours. The reaction was then cooled to room temperature, and the reaction product was transferred to a glass vial. Aqueous HCl solution (10 mL, 6.0 M) was added to the reaction product and sonicated for 1 hour. Afterwards, the solid was collected by centrifugation and washed with distilled water (3 x 10 mL) to remove reaction by-products. The third wash was collected as a colored dispersion of TiC nanocomposite.

Zirconium carbide (ZrC). Using the same method as the preparation of TiC, ZrO_2 (200 mg, 1.62 mmol), biochar (58.5 mg, 4.87 mmol), and Mg (158 mg, 6.50 mmol) were reacted at 950 °C for 8 hours.

Hafnium carbide (HfC). Using the same method as the preparation of TiC NPs, HfO_2 (200 mg, 0.950 mmol), biochar (22.8 mg, 1.90 mmol), and Mg (185 mg, 7.60 mmol) were reacted at 1050 °C for 12 hours.

Characterization techniques. Powder X-ray diffraction (XRD) patterns were collected using a Rigaku Ultima IV X-Ray diffractometer with CuKα radiation (λ = 1.54 A). The samples were placed on to a zero-background silicon wafer and the spectra were collected at 3 counts·s^{-1}. Absorbance spectra were collected using an Agilent CARY 5000 spectrometer. Dispersions were placed in a quartz cuvette and the spectrometer was background corrected using deionized water. Transmission electron microscope (TEM) images were collected using a Thermo Fisher Scientific Talos 200X microscope with an accelerating voltage of 200 kV. HAADF was performed with a spot size less than 1 nm, and a convergence semi-angle of 10.5 mrad. EDS data was acquired using Velox program from Thermo Fisher Scientific. The particle size and lattice spacing were analyzed using ImageJ.[37] Scanning electron microscope (SEM) images were obtained on a Hitachi S-4700 electron microscope. The particles were drop-cast onto a Si wafer. X-ray photoelectron spectroscopy (XPS) analysis was performed on a VG Microtech MultiLab ESCA 2000 X-ray Photoelectron Spectrometer. An Al Kα monochromatic X ray source (1486.6 eV) was used with a system pressure of 10^{-9} Torr. For high resolution scans, a pass energy of 30 eV, energy step of 0.1 eV, and a dwell time of 1000 ms were used. XPS binding energy calibration was done using the C1s peak set to 284.8 eV. This was verified by approximating the location of the Fermi edge using a step-down background type. The position of the Fermi edge, as measured by the intersection of

two straight lines computed from the fitted step-down background, was extracted, and used to estimate an energy offset required to locate the edge position at 0 eV. Spectra corresponding to the same measurement were calibrated by applying the same offset required to calibrate the Fermi edge.[38]

Computational analysis. The absorption spectra of the group 4 carbide NPs were calculated using a finite element method (FEM) solver for Maxwell's equations in COMSOL MultiPhysics. To simulate the optical characteristics of the materials, the real and imaginary parts of dielectric function of the TiC, ZrC, and HfC were obtained from the literature.[34] In simulations, particles were modelled as three dimensional nanospheres suspended in water or embedded in a carbon matrix. To simulate the effect of particle oxidation, metal oxide shells of varying thickness (1, 3, 5, and 10 nm) were placed on particles equal to the corresponding average size for each metal metal carbide. To ensure the accuracy of the results, rigorous convergence analysis and perfectly matched layers (PML) boundary conditions as well as ultra-fine mesh size were utilized in the simulations.[39]

Photothermal efficiency studies. A 365 nm LED source (ThorLabs) with a full width at half-maximum of 10 nm was used as the light source. The illumination power density was calibrated using a silicon photodiode (ThorLabs). The temperature change was monitored using a K-type thermocouple device (EL-USB-TC-LCD, MicroDAQ) with a data logger. A 1.0 cm path length quartz cuvette was used as the container, to which 3.00 mL of the corresponding TMC suspension was added. The solution was stirred constantly using a Teflon-coated magnetic stirring bar. The cuvette was illuminated from the side with an illumination area of 3.0 cm^2. The thermocouple was placed directly into the middle of the solution. Data were collected at 15 seconds intervals for 30

minutes of illumination, followed by cooling. The reported efficiency values were averaged over 5 repetitions.

Results and Discussion

Anatase phase TiO_2, monoclinic ZrO_2, and monoclinic HfO_2 (Figure S1, Supporting Information) with an average particle size of 17 ± 4 nm, 19 ± 5 nm, and 43 ± 10 nm (Figure S2), respectively, were purchased commercially and used without further purification. Biochar was derived from the anaerobic pyrolysis of birch wood chips,[36] followed by treatment with aqueous HNO_3 acid before being rinsed and dried. This was done to increase the surface area and potentially decrease the amount of graphitic carbon, which does not form the carbides under the magnesiothermic reduction reaction conditions.[40–42] The powder XRD pattern was characteristic of amorphous carbon (Figure S3A), and SEM image showed the biochar structures to be micron sized and porous (Figure S3B). Previously, magnesiothermic reduction reactions have been used to form metal carbides below 1000 °C.[36,43–45] Similar process was used in this study, where nanosized metal oxide precursor (TiO_2, ZrO_2 or HfO_2) was ground together with biochar and Mg powder and heated to either 950 °C (TiC, ZrC) or 1050 °C (HfC) under Ar in a tube furnace for 4 – 12 h at a heating rate of 10 °C·min^{-1}. Sonication of the resulting reaction mixture in HCl (6 M) to remove MgO and any unreacted Mg, followed by washing in deionized water afforded the desired carbide nanomaterial.

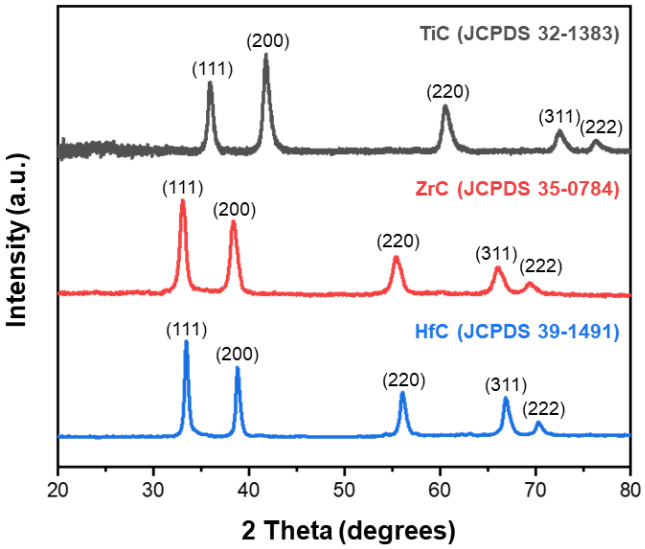

Figure 1. Powder XRD patterns of TiC, ZrC, and HfC nanostructures.

The isolated reaction products were analyzed using powder XRD which showed the formation of cubic phase TiC, ZrC, and HfC (Figure 1).[46–48] A low intensity broad peak was observed centered around ~25° in TiC corresponding to amorphous carbon. Slight trailing of the diffraction peaks was observable in the TiC product which is most likely due to trace amounts of titanium oxycarbide (TiO_xC_y).[49] The surface composition of the TMCs was probed using XPS technique. The high-resolution (HR) XP spectra (Figure S4) of Ti 2p, Zr 3d, and Hf 4f regions showed presence of the corresponding carbide along with oxycarbide (MO_xC_y) and metal oxide (MO_2) peaks indicating surface oxidation of the synthesized TMCs. The presence of the oxycarbide suggests that there is likely a gradient of carbonization between the outer oxide shell and the inner carbide core. HR-XP spectra of C 1s region (Figure S4) showed peaks associated with TiC, ZrC, or HfC in its respective sample. Along with the metal carbide, peaks corresponding to free carbon was also observed in all three products, however, deconvolution of C-C sp^2 and C-

C sp^3 carbon peaks wasn't possible and was fit as one peak. Various oxidized carbon species (alcohol, ketone, carboxylic) were also present in these samples. Peak positions of all species, fitting parameters, and literature references are summarized in Table S1.

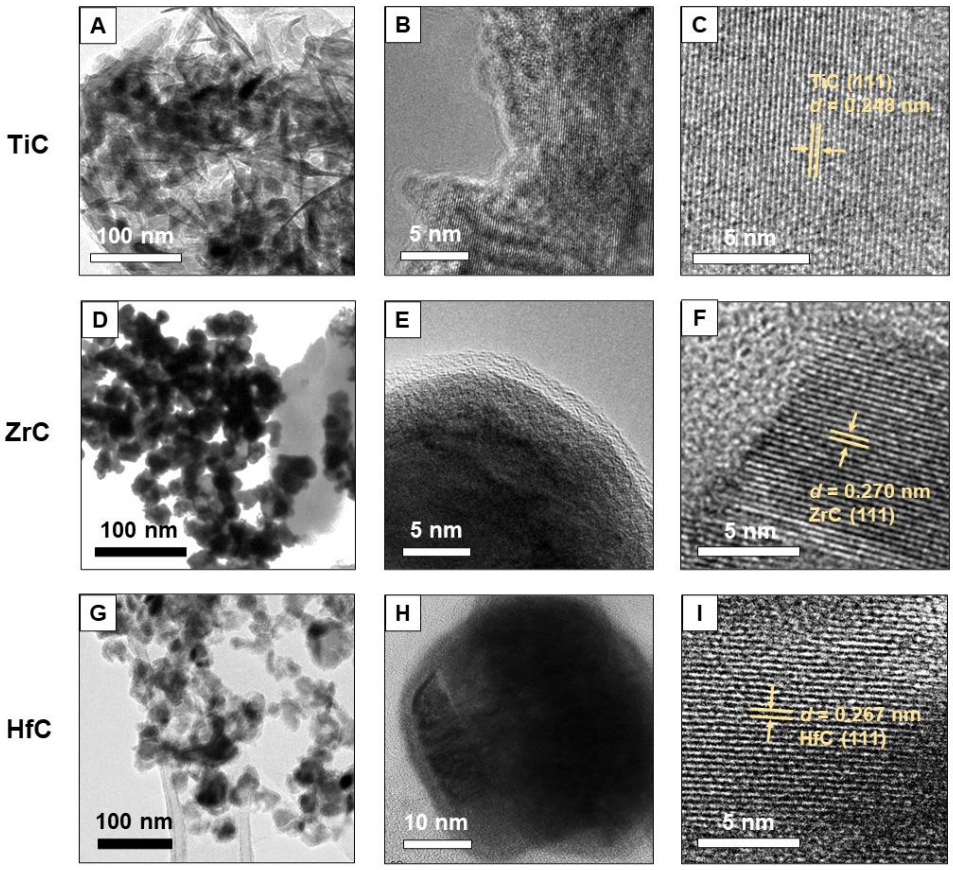

Figure 2. TEM and HRTEM images of (A, B, C) TiC, (D, E, F) ZrC, and (G, H, I) HfC NPs showing particle morphology, amorphous shell surrounding the crystalline carbide core, and lattice spacing.

Figure 2 shows the TEM analysis of the synthesized TMCs (Figure 2). TiC formed the smallest carbide nanostructures with an average particle size of 24 ± 8 nm and were found to be incorporated within an amorphous carbon matrix (Figure 2A). The high resolution (HR) TEM

(Figure 2B) analysis showed presence of crystalline TiC core,[50] surrounded by an amorphous material which can be either from the carbon matrix or particle surface oxide. ZrC sample were comprised of carbide particles with an average size of 31 ± 9 nm along with a few larger (>150 nm) amorphous carbon particles (Figure 2D). The particles had 2 – 3 nm of amorphous shell (Figure 2E) and a crystalline carbide core (Figure 2F).[51] Based on the XPS analysis, the amorphous surface shell is likely metal oxide (ZrO_2) and/or oxycarbide (ZrO_xC_y). Finally, HfC formed from the magnesiothermic reduction were polyhedral with an average size of 42 ± 15 nm (Figure 2G). The particles had an amorphous shell ranging between 2 – 4 nm (Figure 2H) which is likely composed of HfO_2/HfO_xC_y and a crystalline carbide core (Figure 2I).[52] Consistent with the powder XRD patterns, the TEM analysis showed lower amount of carbon impurities in ZrC and HfC compared to TiC. EDS elemental maps confirmed a homogeneous distribution of the metal and carbon throughout each particle (Figure 3). However, oxygen was also found to be throughout the sample possibly from surface oxidation on the TMC NPs and the amorphous carbon. Excess carbon was also observed in TiC sample in regions where the metal was not present consistent with XRD and TEM analysis. Attempts were made to remove the carbon impurities using selective precipitation and chemical etching processes, but these efforts were unsuccessful.

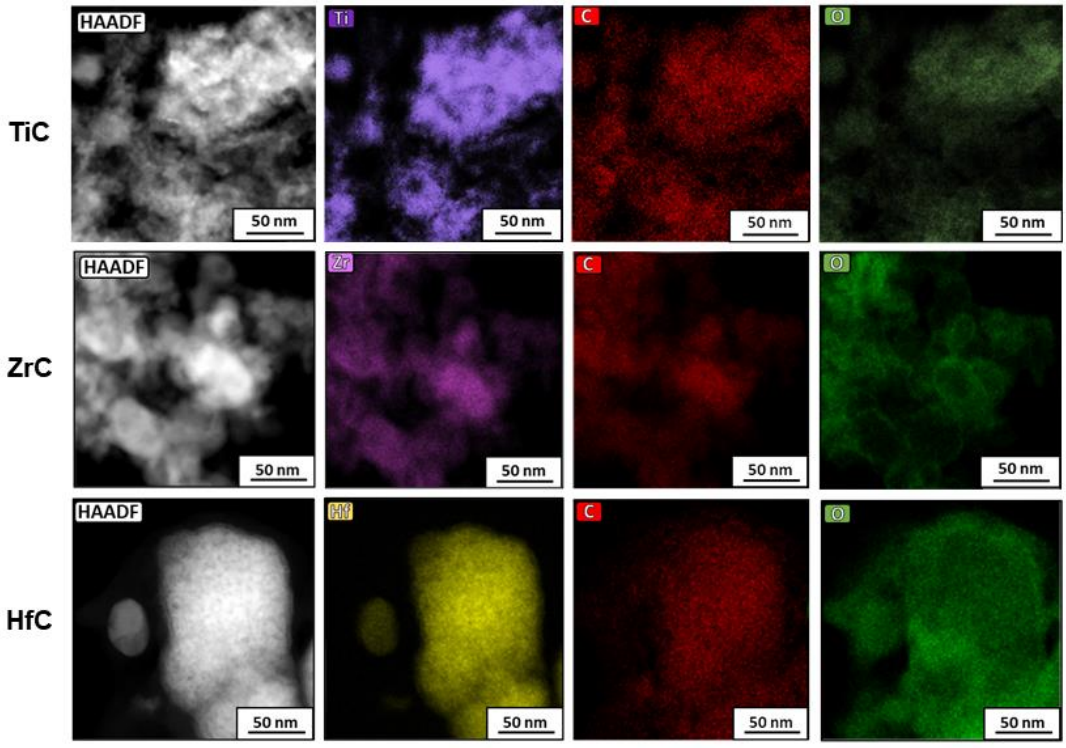

Figure 3. High-angle annular dark field (HAADF) images and EDS elemental maps of TiC, ZrC, and HfC NPs showing the distribution of respective metals (Ti, Zr, Hf), carbon, and oxygen within the samples.

Figure 4 shows the experimental and calculated absorbance spectra for TiC, ZrC, and HfC nanostructures suspended in water. The absorption spectra of free TMC NPs were computed using a finite element method (FEM) and they were assumed to be nanospheres with diameters of 24, 31, and 42 nm for TiC, ZrC, and HfC, respectively. These diameter values represent the average particle size found for each sample by TEM analysis. The calculations showed that the LSPR maximum of TiC, ZrC, and HfC NPs should be located in the UV region centered at 160, 150, and 175 nm, respectively. The LSPR peaks were relatively broad covering most of the UV and parts of the visible region. HfC NPs demonstrated the broadest absorbance peak due to the larger average particle size and increased optical losses.[34] The characteristic LSPR peak could not be observed in

the experimental absorbance spectra due to the spectrophotometer cut-off at 190 nm and the LSPR maximum was predicted to be below that wavelength for all three TMCs. However, a good agreement can be observed between the experimental spectra of ZrC and HfC and their respective calculated absorbance between 200 – 800 nm. Experimentally, a slightly higher absorption was observed in the visible and near-IR region for ZrC and HfC compared to calculations which can be due to the polydispersity of the sample, deviations from the spherical shape of the NPs,[53,54] or the presence of carbon impurities (Figure S5). TiC sample showed a peak at ~290 nm that was redshifted compared to the calculated spectrum. Since TiC sample was found to be mixed with amorphous carbon in the TEM, calculations were performed to compute absorbance of TMC nanostructures embedded in a carbon matrix (Figure S6). The absorption peak of all TMCs broadened and the LSPR maxima redshifted because the carbon matrix has a higher refractive index compared to water.[55] The experimental TiC peak maximum was found to be in between the predicted spectra for NPs suspended in water and embedded within a carbon matrix, indicating that the resonance is likely influenced by both. The calculated absorbance spectra for ZrC and HfC NPs in carbon matrix (Figure S6) were significantly different than the experimental data indicating that the carbon impurities had minimal effect on the frequency of their LSPR. Oxidation of the plasmonic particles can also cause damping of the LSPR, peak broadening, and a redshift in the absorbance peak.[56,57] Calculated spectra of TMCs with varying surface oxide thickness (Figure S7) revealed that carbides don't experience major peak broadening or shifts with increasing oxidation. Slight damping of the LSPR intensity is observed with increasing oxide layer thickness, but not to the extent seen with other classes of plasmonic nanomaterials.[39,56–60] The stability of TMCs over time was monitored by tracking the absorbance of aqueous dispersions of each TMC

material for 150 days. In all cases, no observable changes in the absorbance spectra were noted after 150 days suggesting good long term oxidative stability (Figure S8).

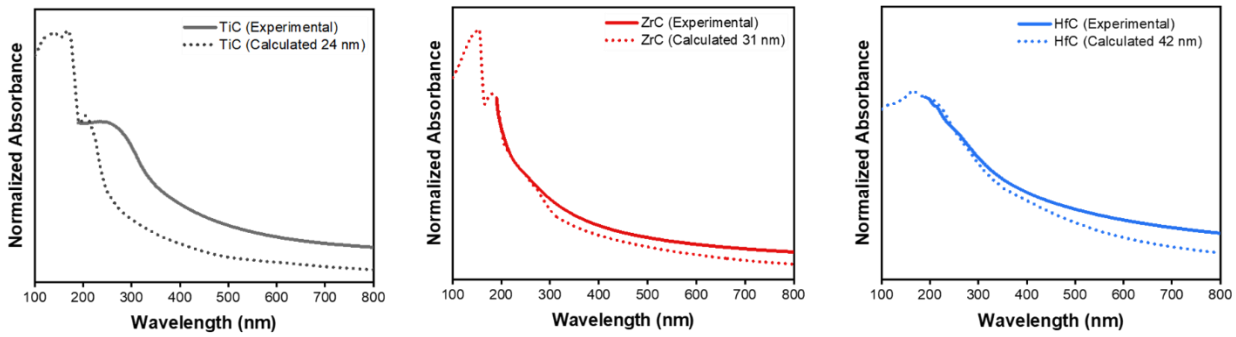

Figure 4. Experimental and calculated absorbance of TiC, ZrC, and HfC NPs suspended in water.

Plasmonic nanomaterials can efficiently convert absorbed light into heat through a phenomenon commonly known as photothermal effect.[61,62] As the absorption maxima of the TMCs fall below the limit of the spectrophotometer, their photothermal behavior was investigated to further validate their plasmonic properties. The photothermal transduction efficiencies were determined for 250 $\mu g \cdot mL^{-1}$ suspensions of each TMC that were excited using a 365 nm LED with a 10 nm bandwidth and 1 $W \cdot cm^{-2}$ illumination intensity (Figure 5A). The nanoparticle solution was continuously illuminated for 30 minutes, allowing it to reach a steady state temperature (Figure 5B). Afterwards, another 30 minutes was allotted to allow the solution to cool back to ambient temperature. The photothermal transduction efficiency was calculated by an energy balance thermal heat transfer method developed by Roper *et al.*[63] using eq 1:

$$\eta_T = \frac{hS(T_{max} - T_{amb}) - Q_0}{I(1 - 10^{-A_\lambda})} \qquad (1)$$

where η_T is the photothermal transduction efficiency, h is the heat transfer coefficient derived from the heating or cooling data (Figure S9), S is the surface area of illumination (3.0 cm^2), T_{max} and T_{amb} are the maximum temperature of the cell and the ambient temperature, respectively, Q_0 is the energy input by the sample cell, I is the incident light intensity, and A_λ is the optical density of the sample solution at the excitation wavelength. In this case, the optical density of the solution is defined as the average absorbance of the corresponding TMC dispersion over the LED bandwidth. HfC achieved the highest change in temperature of 16.5 °C and had the highest transduction efficiency of 73 ± 1% (Figure 3C). Both ZrC (14.5 °C) and TiC (15.0 °C) had comparable temperature increase of 14.5 °C and 15.0 °C, respectively, however the efficiency was higher for ZrC (69 ± 4%) compared to TiC (60 ± 3%). While carbon black also exhibits photothermal effect, its performance wasn't as good as the TMCs under UV-illumination. A temperature change of 5.0 °C and efficiency of 22 ± 2% was observed for the biochar. Even though the oxide precursors absorb light in the UV region, low photothermal transduction efficiency values were observed for TiO_2 (7 ± 1%), ZrO_2 (10 ± 3%), and HfO_2 (12 ± 3%). This further confirms that the high photothermal efficiency values result from the TMC themselves.

To compare the heat generation capabilities and efficiencies of TMCs, the absorption and scattering cross sections at the LED excitation wavelength were calculated. The absorption cross section is directly related to amount of heat generated by the TMCs while the scattering cross section is related to the light-to-heat conversion efficiency. To account for carbon around TiC in the simulations, the average absorption and scattering of TiC NPs with and without carbon around the NPs were used. To account for the LED bandwidth, the calculations were performed using the integral of absorption and scattering over a 10 nm spectral range (360 – 370 nm). As seen in Figure

5D, HfC has the largest absorption cross section within the LED bandwidth, followed by ZrC and TiC. This trend is in agreement with the photothermal heat generation experimental data for the TMCs. The scattering cross section of TiC is significantly larger than ZrC and HfC and this can explain the lower efficiency of TiC in light-to-heat conversion (Figure S10).

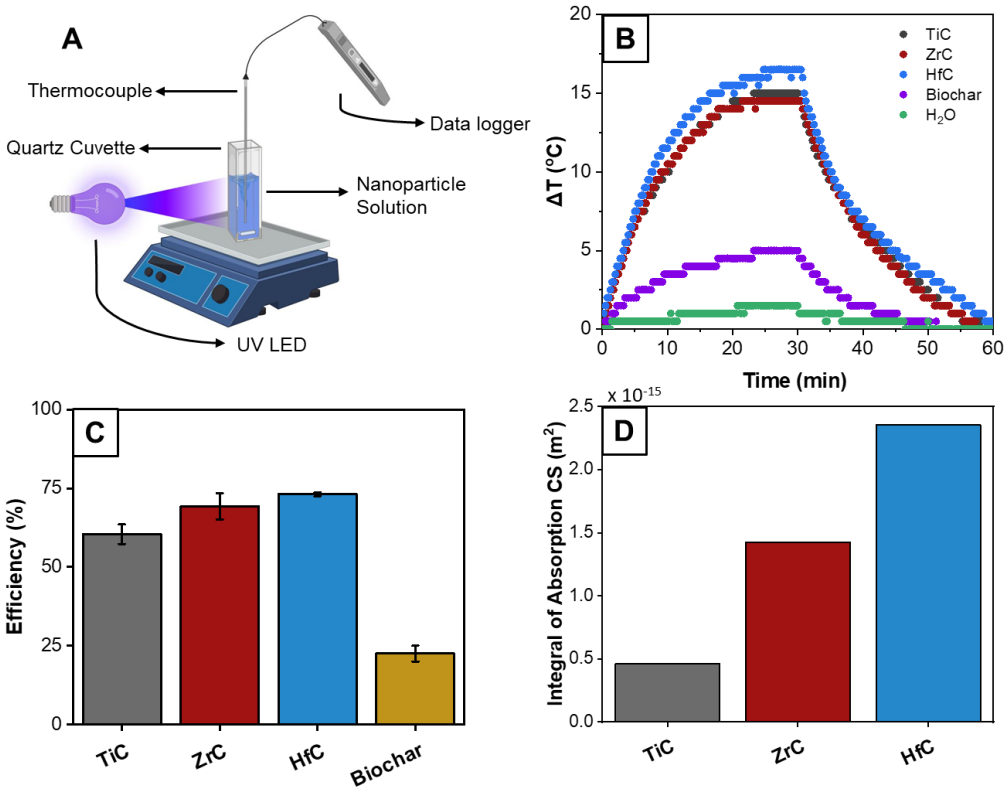

Figure 5. A) Schematic of photothermal heat generation experimental setup. B) Heating and cooling curves for TMCs, biochar, and blank water during photothermal studies. C) Average photothermal transduction efficiencies of TMCs and biochar. D) Calculated absorption cross-section of TMCs between 360 – 370 nm.

Conclusions

UV-plasmonic and water dispersible group IV TMC NPs were prepared using a straightforward magnesiothermic reduction reaction at temperatures between 950 and 1100 °C. TiC, ZrC, and HfC with particle sizes of 24 ± 8, 31 ± 9, and 42 ± 15 nm, respectively and had a crystalline carbide core and an oxide/oxycarbide surface layer. Calculations showed these materials to have LSPR in the deep UV region between 150 – 175 nm. While a distinctive LSPR was not observed in absorbance data due to spectrometer wavelength cutoff, photothermal studies showed these materials to possess high efficiencies typical of plasmonic nanostructures. Upon excitation with 365 nm LED source, TiC, ZrC, and HfC had an average photothermal transduction efficiency of 60, 69, and 73%, respectively. The NPs suspension exhibited good stability overtime with negligible change in their optical response over 150 days. The plasmonic response in the UV region combined with the high photothermal efficiencies make TMCs attractive for disinfection, biological imaging, and sensing. The synthetic method reported here is scalable and can be extended to prepare other plasmonic carbides as well.

Conflicts of interest

There are no conflicts to declare.

Electronic Supplementary Information

See supplementary material for Figures S1 – S10 and Table S1.

Acknowledgements

The authors acknowledge funding from Canada Foundation for Innovation (CFI) and Natural Sciences and Engineering Research Council of Canada (NSERC). Dr. Carmen Andrei and Canadian Center for Microscopy are thanked for assistance with the TEM and EDS mapping experiments. CMC Microsystems is thanked for the access to COMSOL software. Dr. Andrew George is thanked for assistance with XPS measurements. YEM thanks postdoctoral fellowship from Ocean Frontier Institute (OFI) and MM for graduate fellowship from Sumner Foundation.

References

1 S. Link and M. A. El-Sayed, Shape and size dependence of radiative, non-radiative and photothermal properties of gold nanocrystals, *Int. Rev. Phys. Chem.*, 2000, **19**, 409–453.

2 Z.-Q. Tian, B. Ren and D.-Y. Wu, Surface-enhanced raman scattering: From noble to transition metals and from rough surfaces to ordered nanostructures, *J. Phys. Chem. B*, 2002, **106**, 9463–9483.

3 S. A. Maier and H. A. Atwater, Plasmonics: Localization and guiding of electromagnetic energy in metal/dielectric structures, *J. Appl. Phys.*, 2005, **98**, 11101.

4 P. K. Jain, X. Huang, I. H. El-Sayed and M. A. El-Sayed, Noble metals on the nanoscale: Optical and photothermal properties and some applications in imaging, sensing, biology, and medicine, *Acc. Chem. Res.*, 2008, **41**, 1578–1586.

5 Z.-Y. Li, Mesoscopic and microscopic strategies for engineering plasmon-enhanced raman scattering, *Adv. Opt. Mater.*, 2018, **6**, 1701097.

6 W. A. Murray and W. L. Barnes, Plasmonic materials, *Adv. Mater.*, 2007, **19**, 3771–3782.

7 S. V Boriskina, H. Ghasemi and G. Chen, Plasmonic materials for energy: From physics to applications, *Mater. Today*, 2013, **16**, 375–386.

8 D. K. Gramotnev and S. I. Bozhevolnyi, Plasmonics beyond the diffraction limit, *Nat. Photonics*, 2010, **4**, 83–91.

9 Z. Zhao, Y. Luo, W. Zhang, C. Wang, P. Gao, Y. Wang, M. Pu, N. Yao, C. Zhao and X. Luo, Going far beyond the near-field diffraction limit via plasmonic cavity lens with high spatial frequency spectrum off-axis illumination, *Sci. Rep.*, 2015, **5**, 15320.

10 S. Alekseeva, I. I. Nedrygailov and C. Langhammer, Single particle plasmonics for materials science and single particle catalysis, *ACS Photonics*, 2019, **6**, 1319–1330.

11 V. Amendola, R. Pilot and M. Frasconi, Surface plasmon resonance in gold nanoparticles : A review, *J. Phys. Condens. Matter.*, 2017, **29**, 1–48.

12 M. Song, D. Wang, Z. A. Kudyshev, Y. Xuan, Z. Wang, A. Boltasseva, V. M. Shalaev and A. V Kildishev, Enabling optical steganography, data storage, and encryption with plasmonic colors, *Laser Photon. Rev.*, 2021, **15**, 2000343.

13 M. Dhiman, Plasmonic nanocatalysis for solar energy harvesting and sustainable chemistry, *J. Mater. Chem. A*, 2020, **8**, 10074–10095.

14 A. Naldoni, U. Guler, Z. Wang, M. Marelli, F. Malara, X. Meng, L. V Besteiro, A. O. Govorov, A. V Kildishev, A. Boltasseva and V. M. Shalaev, Broadband hot-electron collection for solar water splitting with plasmonic titanium nitride, *Adv. Opt. Mater.*, 2017, **5**, 1601031.

15 F. Zhao, Y. Guo, X. Zhou, W. Shi and G. Yu, Materials for solar-powered water evaporation, *Nat. Rev. Mater.*, 2020, **5**, 388–401.

16 L. Zhu, M. Gao, C. K. N. Peh and G. W. Ho, Recent progress in solar-driven interfacial water evaporation: Advanced designs and applications, *Nano Energy*, 2019, **57**, 507–518.

17 Y. Pang, J. Zhang, R. Ma, Z. Qu, E. Lee and T. Luo, Solar–thermal water evaporation: A review, *ACS Energy Lett.*, 2020, **5**, 437–456.

18 C. Zhang, H.-Q. Liang, Z.-K. Xu and Z. Wang, Harnessing solar-driven photothermal effect toward the water–energy nexus, *Adv. Sci.*, 2019, **6**, 1900883.

19 M. J. Margeson and M. Dasog, Plasmonic metal nitrides for solar-driven water evaporation, *Environ. Sci. Water Res. Technol.*, 2020, **6**, 3169–3177.

20 U. Aslam, V. G. Rao, S. Chavez and S. Linic, Catalytic conversion of solar to chemical energy on plasmonic metal nanostructures, *Nat. Catal.*, 2018, **1**, 656–665.

21 E. A. Monyoncho and M. Dasog, Photocatalytic plasmon-enhanced nitrogen reduction to ammonia, *Adv. Energy Sustain. Res.*, 2021, **2**, 2000055.

22 O. S. Kolovskaya, T. N. Zamay, I. V Belyanina, E. Karlova, I. Garanzha, A. S. Aleksandrovsky, A. Kirichenko, A. V Dubynina, A. E. Sokolov, G. S. Zamay, Y. E. Glazyrin, S. Zamay, T. Ivanchenko, N. Chanchikova, N. Tokarev, N. Shepelevich, A. Ozerskaya, E. Badrin, K. Belugin, S. Belkin, V. Zabluda, A. Gargaun, M. V Berezovski and A. S. Kichkailo, Aptamer-targeted plasmonic photothermal therapy of cancer, *Mol. Ther. Nucleic Acid*, 2017, **9**, 12–21.

23 M. Kim, J.-H. Lee and J.-M. Nam, Plasmonic photothermal nanoparticles for biomedical

applications, *Adv. Sci.*, 2019, **6**, 1900471.

24 M. R. K. Ali, Y. Wu and M. A. El-Sayed, Gold-nanoparticle-assisted plasmonic photothermal therapy advances toward clinical application, *J. Phys. Chem. C*, 2019, **123**, 15375–15393.

25 G. V Naik, V. M. Shalaev and A. Boltasseva, Alternative plasmonic materials: beyond gold and silver, *Adv. Mater.*, 2013, **25**, 3264–3294.

26 W. He, K. Ai, C. Jiang, Y. Li, X. Song and L. Lu, Plasmonic titanium nitride nanoparticles for in vivo photoacoustic tomography imaging and photothermal cancer therapy, *Biomaterials*, 2017, **132**, 37–47.

27 G. V Naik, J. Kim and A. Boltasseva, Oxides and nitrides as alternative plasmonic materials in the optical range, *Opt. Mater. Express*, 2011, **1**, 1090–1099.

28 S. Magdi and M. A. Swillam, Investigating several ZrN plasmonic nanostructures and their effect on the absorption of organic solar cells, *J. Phys. D. Appl. Phys.*, 2017, **50**, 385501.

29 S. Venkataramanababu, G. Nair, P. Deshpande, M. A. Jithin, S. Mohan and A. Ghosh, Chiro-plasmonic refractory metamaterial with titanium nitride (TiN) core-shell nanohelices, *Nanotechnology*, 2018, **29**, 255203.

30 S. Juneja and M. S. Shishodia, Surface plasmon amplification in refractory transition metal nitrides based nanoparticle dimers, *Opt. Commun.*, 2019, **433**, 89–96.

31 U. Guler, A. Boltasseva and V. M. Shalaev, Refractory plasmonics, *Science.*, 2014, **344**, 263–264.

32 M. Dasog, Transition metal nitrides are heating up the field of plasmonics, *Chem. Mater.*, 2022, **34**, 4249–4258.

33 R. A. Karaballi, Y. E. Monfared and M. Dasog, Overview of synthetic methods to prepare plasmonic transition-metal nitride nanoparticles, *Chem. – A Eur. J.*, 2020, **26**, 8499–8505.

34 M. Kumar, N. Umezawa, S. Ishii and T. Nagao, Examining the performance of refractory conductive ceramics as plasmonic materials: A theoretical approach, *ACS Photonics*, 2016, **3**, 43–50.

35 S. Ai, M. Ma, Y.-Z. Chen, X.-H. Gao and G. Liu, Metal-ceramic carbide integrated solar-driven evaporation device based on ZrC nanoparticles for water evaporation and desalination, *Chem. Eng. J.*, 2022, **429**, 132014.

36 G. Humagain, K. MacDougal, J. MacInnis, J. M. Lowe, R. H. Coridan, S. MacQuarrie and M. Dasog, Highly efficient, biochar-derived molybdenum carbide hydrogen evolution electrocatalyst, *Adv. Energy Mater.*, 2018, **8**, 1801461.

37 C. A. Schneider, W. S. Rasband and K. W. Eliceiri, NIH Image to ImageJ: 25 years of image analysis, *Nat. Methods*, 2012, **9**, 671–675.

38 G. Greczynski and L. Hultman, X-ray photoelectron spectroscopy: Towards reliable binding energy referencing, *Prog. Mater. Sci.*, 2020, **107**, 100591.

39 Y. Esfahani Monfared and M. Dasog, Computational investigation of the plasmonic properties of TiN, ZrN, and HfN nanoparticles: the role of particle size, medium, and surface oxidation, *Can. J. Chem.*, 2020, **99**, 576–584.

40 A. Anstey, S. Vivekanandhan, A. Rodriguez-Uribe, M. Misra and A. K. Mohanty,

Oxidative acid treatment and characterization of new biocarbon from sustainable Miscanthus biomass, *Sci. Total Environ.*, 2016, **550**, 241–247.

41 C. Peiris, O. Nayanathara, C. M. Navarathna, Y. Jayawardhana, S. Nawalage, G. Burk, A. G. Karunanayake, S. B. Madduri, M. Vithanage, M. N. Kaumal, T. E. Mlsna, E. B. Hassan, S. Abeysundara, F. Ferez and S. R. Gunatilake, The influence of three acid modifications on the physicochemical characteristics of tea-waste biochar pyrolyzed at different temperatures: a comparative study, *RSC Adv.*, 2019, **9**, 17612–17622.

42 C. Liu, W. Wang, R. Wu, Y. Liu, X. Lin, H. Kan and Y. Zheng, Preparation of acid- and alkali-modified biochar for removal of methylene blue pigment, *ACS Omega*, 2020, **5**, 30906–30922.

43 N. Hidayat, Ardiansyah, A. Fuad, N. Mufti, A. A. Fibriyanti, C. I. Yogihati and B. Prihandoko, Magnesiothermic reduction synthesis of silicon carbide with varying temperatures: Structural and mechanical features, *IOP Conf. Ser. Mater. Sci. Eng.*, 2019, **515**, 12012.

44 O. Torabi, M. H. Golabgir, H. Tajizadegan and H. Torabi, A study on mechanochemical behavior of MoO3–Mg–C to synthesize molybdenum carbide, *Int. J. Refract. Met. Hard Mater.*, 2014, **47**, 18–24.

45 P. Asgarian, A. Nourbakhsh, P. Amin, R. Ebrahimi-Kahrizsangi and K. J. D. MacKenzie, The effect of different sources of porous carbon on the synthesis of nanostructured boron carbide by magnesiothermic reduction, *Ceram. Int.*, 2014, **40**, 16399–16408.

46 *International Center for Diffraction Data 32-1383*, .

47 *International Center for Diffraction Data 35-0784*, .

48 *International Center for Diffraction Data 39-1491*, .

49 Z. Xie, Y. Deng, Y. Yang, H. Su, D. Zhou, C. Liu and W. Yang, Preparation of nano-sized titanium carbide particles via a vacuum carbothermal reduction approach coupled with purification under hydrogen/argon mixed gas, *RSC Adv.*, 2017, **7**, 9037–9044.

50 F. Saba, F. Zhang, S. A. Sajjadi and M. Haddad-Sabzevar, in *Spark Plasma Sintering of Materials: Advances in Processing and Applications*, ed. P. Cavaliere, Springer International Publishing, Cham, 2019, pp. 119–159.

51 B. Wei, D. Wang, Y. Wang, H. Zhang, S. Peng, C. Xu, G. Song and Y. Zhou, Corrosion kinetics and mechanisms of ZrC1−x ceramics in high temperature water vapor, *RSC Adv.*, 2018, **8**, 18163–18174.

52 X. Gu, L. Yang, X. Ma, X. Dai, J. Wang, M. Wen and K. Zhang, Ta addition effects on the structure, mechanical and thermal properties of sputtered Hf-Ta-C film, *Ceram. Int.*, 2019, **45**, 15596–15602.

53 H. Tang, C. Zhu, G. Meng and N. Wu, Review - Surface-enhanced raman scattering sensors for food safety and environmental monitoring, *J. Electrochem. Soc.*, 2018, **165**, B3098–B3118.

54 C. L. Nehl and J. H. Hafner, Shape-dependent plasmon resonances of gold nanoparticles, *J. Mater. Chem.*, 2008, **18**, 2415–2419.

55 B. J. Stagg and T. T. Charalampopoulos, Refractive indices of pyrolytic graphite, amorphous carbon, and flame soot in the temperature range 25° to 600°C, *Combust.*

Flame, 1993, **94**, 381–396.

56 A. Ziashahabi and R. Poursalehi, The effects of surface oxidation and interparticle coupling on surface plasmon resonance properties of aluminum nanoparticles as a UV plasmonic material, *Procedia Mater. Sci.*, 2015, **11**, 434–437.

57 A. Kuzma, M. Weis, S. Flickyngerova, J. Jakabovic, A. Satka, E. Dobrocka, J. Chlpik, J. Cirak, M. Donoval, P. Telek, F. Uherek and D. Donoval, Influence of surface oxidation on plasmon resonance in monolayer of gold and silver nanoparticles, *J. Appl. Phys.*, 2012, **112**, 103531.

58 C. J. Powell and J. B. Swan, Effect of Oxidation on the Characteristic Loss Spectra of Aluminum and Magnesium, *Phys. Rev.*, 1960, **118**, 640–643.

59 O. A. Douglas-Gallardo, G. J. Soldano, M. M. Mariscal and C. G. Sánchez, Effects of oxidation on the plasmonic properties of aluminum nanoclusters, *Nanoscale*, 2017, **9**, 17471–17480.

60 Y. Fang, Z. Cheng, S. Wang, H. Hao, L. Li, S. Zhao, X. Chu and R. Zhu, Effects of oxidation on the localized surface plasmon resonance of Cu nanoparticles fabricated via vacuum coating, *Vacuum*, 2021, **184**, 109965.

61 S. Manrique-Bedoya, M. Abdul-Moqueet, P. Lopez, T. Gray, M. Disiena, A. Locker, S. Kwee, L. Tang, R. L. Hood, Y. Feng, N. Large and K. M. Mayer, Multiphysics modeling of plasmonic photothermal heating effects in gold nanoparticles and nanoparticle arrays, *J. Phys. Chem. C*, 2020, **124**, 17172–17182.

62 S. J. Norton and T. Vo-Dinh, Photothermal effects of plasmonic metal nanoparticles in a

fluid, *J. Appl. Phys.*, 2016, **119**, 83105.

63 D. K. Roper, W. Ahn and M. Hoepfner, Microscale heat transfer transduced by surface plasmon resonant gold nanoparticles, *J. Phys. Chem. C*, 2007, **111**, 3636–3641.